Advanced Steel Construction – Vol. 19 No. 2 (2023) 130–142
DOI:10.18057/IJASC.2023.19.2.5

MOMENT-ROTATION MODEL OF EXTERNAL COVER PLATE JOINTS BETWEEN STEEL BEAMS AND CONCRETE-FILLED SQUARE STEEL TUBULAR COLUMNS WITH INNER I-SHAPED CFRP PROFILE

Guo-Chang Li [1], Ming-Hao Shen [1,*], Da-Cang Ji [1], Han-Bin Ge [2] and Xu Liu [1]

[1] *School of Civil Engineering, Shenyang Jianzhu University, Shenyang, Liaoning 110168, China*
[2] *Department of Civil Engineering, Meijo University, Nagoya, Aichi 468-8502, Japan*
** (Corresponding author: E-mail: shenminghao96@163.com)*

ABSTRACT

As a new type of beam-column joint, external cover plate joints can be used in concrete-filled square steel tubular (CFSST) structures. To accurately analyze the mechanical characteristics of this novel joint during structural design, it is necessary to investigate the moment-rotation relationships. Based on the analysis of the force-transferring mechanism, the formulas to decide the initial rotation stiffness and ultimate bending moment are founded by using the component analysis method, while the finite element analysis results are also utilized to verify these formulas. Considering the advantages and disadvantages of the existing typical moment-rotation models, a new representation for calculating the moment-rotation curve of the external cover plate joints is proposed using the ultimate bending moment and initial rotation stiffness as two basic parameters. The research reveals that the moment-rotation model proposed in this paper is able to take all loading stages of this joint into account, which facilitates the analysis of yield and ultimate loads. In addition, this model is smooth and continuous at the piecewise points to avoid numerical problems that may be caused in the calculation. Comparing the moment-rotation curves obtained by the calculation model and finite element simulation, the results show good consistency, demonstrating that the moment-rotation model presented in this paper is applicable to the analysis and design of the external cover plate joints.

ARTICLE HISTORY

Received: 13 May 2022
Revised: 11 July 2022
Accepted: 20 July 2022

KEYWORDS

Concrete-filled square steel tubular;
External cover plate joint;
I-shaped CFRP profile;
Initial rotational stiffness;
Ultimate bending moment;
Component method;
Moment-rotation model

1. Introduction

Concrete-filled steel tubular (CFST) members have seen increased use in actual engineering over the last few years for their high strength and ductility [1]. To further improve the mechanical properties of the structures and reduce the section size of the columns, the author's team proposed to put an I-shaped CFRP profile in the CFST member, taking full advantage of three materials, namely concrete, steel, and CFRP profile [2-4]. According to the seismic design principle, the structures should remain stable under seismic loads. During the process of resisting the earthquake, the joints between columns and beams should provide sufficiently large strength and stiffness to survive the structures under the earthquake. Therefore, the structural form and mechanical properties of the joints have always been the focus of many scholars. Among the main forms of beam-column joints, the joints with external diaphragms have the advantages of clear force transmission, good plasticity, high bearing capacity, and strong energy dissipation capacity [5-8]. Because of its own structural characteristics, this joint enables the plastic hinge to occur first in the beam section, allowing the beam to dissipate energy during the seismic event and thus ensure the column does not lose its load-bearing capacity [9,10]. However, due to a large amount of on-site construction work and high requirements for weld quality, the external diaphragm joints are rarely used. To solve the problem of low usage of the external diaphragm joints, our team proposed an external cover plate joint suitable for connecting concrete-filled square steel tubular (CFSST) columns and I-shaped steel beams. The proposed joint not only reduces the amount of on-site construction work but also solves the problem of matching the size of the external diaphragm with the column section in the traditional external diaphragm joints. Moreover, this joint has the same benefits of clear and reliable force transmission as the traditional external diaphragm joints.

All joints applied in practical engineering exhibit varying degrees of semi-rigid characteristics. However, in structural design, beam-column joints are usually simply regarded as completely rigid or hinged, so that only the moment resistance of joints is calculated, the rotational stiffness, which plays a crucial role in the stress distribution and deformation of the structure, is ignored [11,12]. Therefore, a thorough understanding of the rotational stiffness is necessary for accurate structural analysis. The moment-rotation relationship enables us to consider the rotation of the joints in structural analysis, so as to accurately analyze the story displacement of the structure [13]. Although an approximately accurate moment-rotation relationship captured from experiments or finite element simulations is available, they require high economic or time costs. Therefore, the insufficiency of experiments and simulations is generally filled by founding theoretical models. In recent years, several influential moment-rotation curve models have been proposed by numerous scholars. Ding et al. [14] put forward an improved bilinear model, which was practical to use in design because the mechanical behavior of a beam-column joint can be predicted by only two parameters. Wu et al. [15] proposed a three-parameter exponential function in which a shape-coefficient was introduced to adjust the overall shape of the curve. Yee et al. [16] presented a four-parameter exponential function that predicted the ultimate state of joints by introducing the strain hardening stiffness. Frye et al. [17] proposed a polynomial model by fitting multiple sets of experimental data with the least squares method. Colson [18] and Kishi [19] proposed power function models to obtain the ultimate bending moment of joints by solving asymptotes. To achieve a more precise mathematical model, Ang et al. [20] recommended a four-parameter power function model based on the Ramberg-Osgood function. The existing moment-rotation models can generally be classified into two types: piecewise function models and single nonlinear function models. The piecewise function model is prone to abrupt changes at the breakpoints, which may lead to numerical problems such as computational non-convergence in the subsequent analysis. In contrast, the single nonlinear function model has no clear definition for all loading stages of joints.

In this study, we analyzed the force-transferring mechanism of the proposed joint through numerical simulations. Additionally, the component method is introduced to analyze the external cover plate joint. To accomplish this objective, the force-transferring mechanism of the basic components is identified and clarified. Then, the calculation formulas for ultimate flexural capacity and initial rotation stiffness are derived utilizing the principle of the component method. Finally, considering the advantages and disadvantages of the typical moment-rotation models, according to the ultimate flexural capacity and initial rotation stiffness as two primary factors, a novel mathematical representation is presented to determine the moment-rotation relationship. The research results obtained in this paper can improve the design theory of this type of joint and provide a research basis for its application to concrete-filled square steel tubular structures.

2. Connection details and finite element model

In this section, we presented the specific details of the external cover plate joint and discussed the method of building a fine finite element model using the nonlinear analysis software ABAQUS.

2.1. Connection details

To solve the problem with the low usage of external diaphragm joints, our research group has proposed the external cover plate joint. The main components of this joint are cover plates, angle steels, and high-strength bolts. Compared with the traditional external diaphragm joint, this novel joint solves

the installation inconvenience caused by the deviation between the opening size of external diaphragms and the section size of columns, achieving the detachable connection and thus meeting the requirements of the fabricated building. Fig. 1(a) presents the overall schematic of the joint.

Every part of the joint can be prefabricated in the factory. The cover plate can be pre-welded to the upper flange of the beam before on-site assembly. Also, the angle steels are connected to the steel tube by fillet welds in advance. When assembling on-site, the cover plates and lower angle steels are connected by high-strength bolts in advance as temporary support for subsequent assembly, and the upper angle steel plays a positioning role. After the beam and column are lapped, the cover plates are connected with the upper angle steel by high-strength bolts. Finally, the welding work between the cover plate and the lower flange of the beam as well as the welding work between the beam web and the square steel tube are carried out. It is worth noting that all cover plates and steel tube are not welded. The assembly process is shown in Fig. 1(b).

The sizes of the base model (JZ-1) for finite element model analysis are as follows: The section size of the composite column is 250 × 250 mm^2, the wall thickness is 10mm, and the height is 3000mm; The beam is made of 300 × 150 × 6.5 × 9 mm I-steel, and the length is 1500 mm; The section size of angle steel is L90 × 10 mm, and the length is 770 mm; The cover plate size is 430 × 260 × 10 mm. According to the relevant design references [21-23], the sizes of the joint were checked, and the joint met the design principle of "strong column and weak beam, strong connection and weak members". Grade 10.9 M20 high-strength bolts are adopted for all connecting bolts. Each component's material strength of the joint is shown in Table 1. The specific size of the finite element model is shown in Fig. 2.

Table 1
Material strength

Materials	Steel tube	Concrete	Beam	Angle steel	Cover plate
Strength	Q460	C60	Q355	Q355	Q355

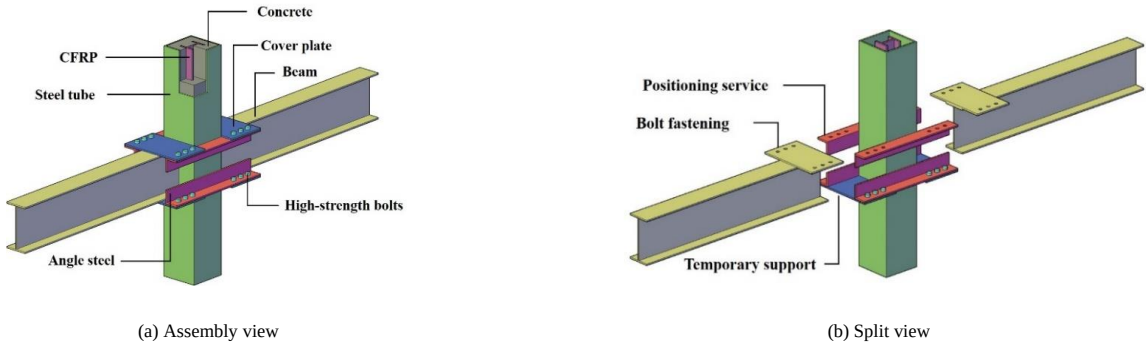

(a) Assembly view (b) Split view

Fig. 1 External cover plate connection overview

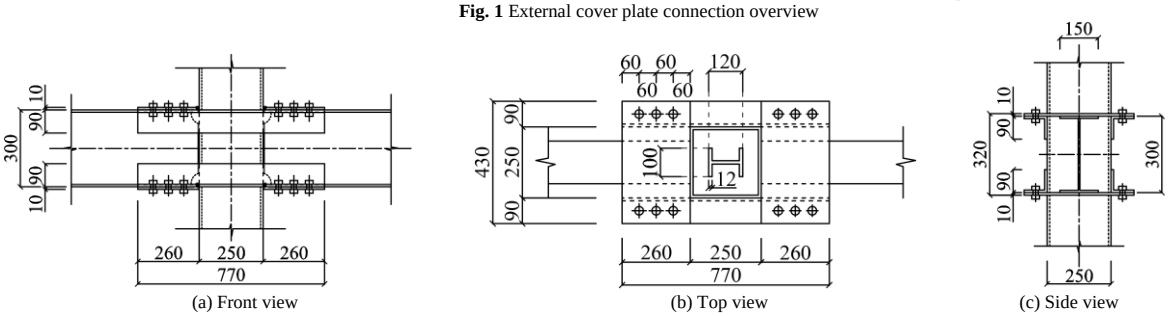

(a) Front view (b) Top view (c) Side view

Fig. 2 Details of the specimens

2.2. Refined finite element model

2.2.1. Material constitutive model

Considering the confinement effect of the square steel tube, the constitutive relation of infilled concrete proposed by Han [24] is adopted in this paper, with the range of application being f_{cu} = 30~120 MPa, f_y = 200~700 Mpa. A trilinear model considering the strengthening stage and the descending stage was used for the constitutive relation of steel. The I-shaped CFRP profile was made of internal unidirectional carbon fiber and external bi-directional carbon fiber by the pultrusion process, so it could be regarded as a three-layer orthogonal anisotropic material. A subroutine based on a secondary development in ABAQUS was utilized to define the CFRP material characteristics, and the Tsai-Wu failure criterion was used to discriminate whether its elements were damaged.

2.2.2. Contact analysis model

A frictional contact with a friction coefficient of 0.6 was used in the tangential direction for producing the contact surface between the square steel tube and the infilled concrete. Hard contact was used to mimic the contact behavior in the normal direction. The same settings were also applied to the contact surfaces between the cover plates, angle steels and high-strength bolts, except the tangential friction coefficient was 0.45. Tie restraint was used at the contact surface between the I-shaped CFRP profile and the concrete because the experimental results in [25,26] showed no relative sliding between the CFRP profile and concrete after loading. The cover plates and beam flanges were not welded with the steel tube, so the contact relationship between each of them and the steel tube was simulated by the "friction" and "hard" contacts with a friction coefficient of 0.45. Fillet welds were adopted for the connection between the angle steels/beam webs and the steel tube, so the tie constraints were applied between angle steels, beam webs and the steel tube. Similarly, the fillet welds were adopted between the cover plates and the beam flanges, because the contact relationship between them was taken as the tie constraint.

2.2.3. The boundary conditions and meshing

Fig. 3 shows the boundary conditions and meshing of the numerically simulated model. To avoid the occurrence of out-of-plane instability, the constraints of the lateral support on the beam were simulated by limiting the degrees of freedom along the Y-direction in the end section of the beam. Only the degree of freedom in the Z-direction on the top of the column was not restrained and applying an axial load (N_0) with an axial load ratio of 0.3 to the top of the column. Fixed restraint was used at the bottom of the column.

The I-shaped CFRP profile was modeled by the SC8R (continuous shell element), and a sweeping mesh method was adopted with the sweeping paths following the thickness direction of the flange and web respectively. Besides, concrete, steel tube, cover plates, angle steels, and beams were modeled by the C3D8R (eight-node reduced integral solid element). The meshing method used the structural mesh method. In addition, the panel area and the beam section connected to the cover plate were divided more intensively in the meshing.

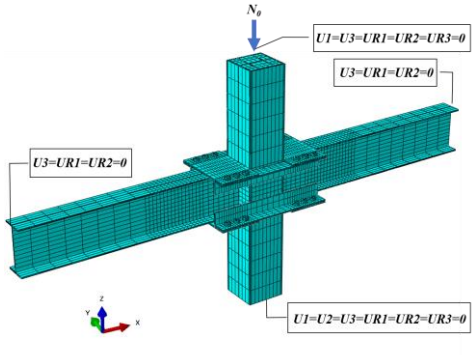

Fig. 3 Boundary conditions and meshing

2.2.4. Accuracy verification of finite element model

To assess the validity of the modeling approach, a few specimens from the current references [27,28] were simulated using the aforementioned finite element modeling technique. Fig . 4 compared the experimental and finite element simulation findings. It can be seen that the simulation results closely match the curves provided in the references. In summary, the finite element modeling method presented in this paper is precise and can be applied for subsequent analysis.

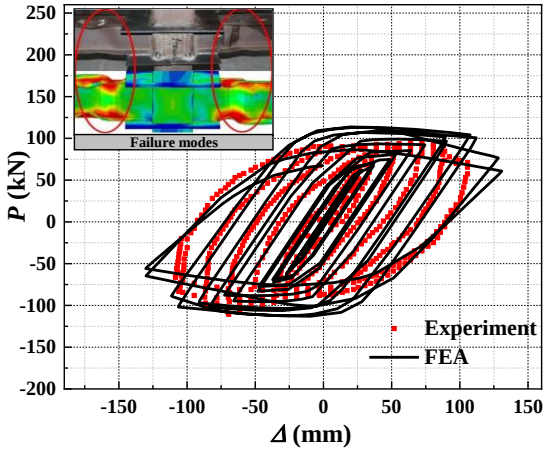

(a) Comparison with the hysteresis curves in [27]

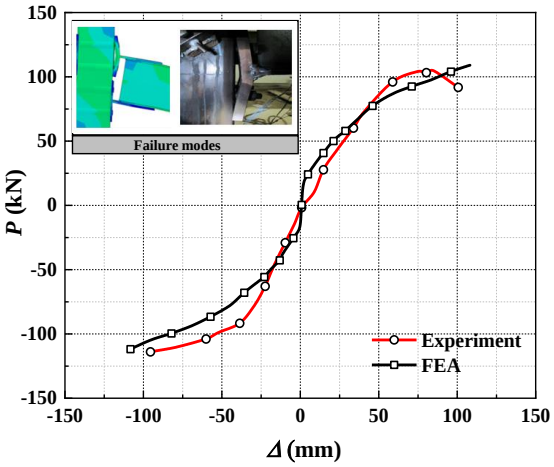

(b) Comparison with the skeleton curves in [28]

Fig. 4 Verification of finite element modeling method

3. Transfer mechanism analysis

In this study, it is considered that the bending moment applied to the beam can be decomposed into a set of horizontal loads on the beam flanges and the vertical load on the beam web, which is transferred to the panel zone of the combined column through the connectors. Therefore, based on the analysis of the distribution of horizontal and vertical stresses on the steel beam, cover plate, angle steel, and steel tube, this section discusses the force transmission mechanism of such composite joints.

In addition, since the stress distribution on each member does not change significantly from the beginning of loading to the peak load stage and only the stress value changes, the analysis can reveal the transmission mechanism of the joint by selecting a specific moment in the loading process.

3.1. Horizontal stress distribution

3.1.1. Horizontal stress distribution of steel beam

Fig. 5(a) reveals that, aside from the beam flange, the bending moment at the beam end can be resolved into a set of horizontal loads of equal magnitude and opposite directions acting on the beam web. When the shear force is exerted on the beam section, a distinct area of tension and compression forms at the beam web.

In ABAQUS, the path analysis approach was utilized to examine the horizontal stress distribution in the beam flange and web section. According to Fig. 6(a), point B is the position of the cross-section where the stress mutation occurs on the beam flange, and point A is the location of the cross-section where the beam flange is connected to the cover plate. It is observed that the curve at point B has a mutation, and the mutation position is about x = 300 mm. Compared with the upper flange of the steel beam, the position where the stress mutation of the lower flange is more obvious, indicating that the plastic deformation of the lower flange is more significant. The flange of the steel beam began to connect with the cover plate at point A, and the stress began to decrease rapidly after passing point A, indicating that the horizontal stress passed through the beam flange to the cover plate. In addition, the horizontal stress at the beam web starts to decline before reaching point A, indicating that the tensile and compressive forces at the web of the steel beam are first introduced into the beam flange and then transferred to the cover plate.

3.1.2. Horizontal stress distribution of cover plate

In Fig. 5(b), the transmission path of principal stress at the cover plate shows that the stress on the cover plate mainly comes from the flange of the steel beam and continues to be transmitted to the bolt holes along the 45° oblique direction.

Since the stress distribution of the cover plate is almost the same when it is in tension and compression, only the tensile stress distribution in different sections of the cover plate was analyzed, as shown in Fig. 6(b). It can be seen that the tensile stress in section ‘1-1’ is the largest between the area of x = 140 mm and 290 mm, which is because the beam flange is connected with the edge of the cover plate, and the tensile stress on the beam flange is transferred to the cover plate from this region. According to the figure, as the section position shifts from ‘1-1’ to ‘6-6’, the location of the maximum tensile stress shifts outward from x = 215.2 mm to 139.9 mm, indicating that the tensile stress on the cover is mainly transferred to the bolt holes in the oblique direction. Due to the stress concentration at the bolt hole, the stress values of the curve at x = 45 mm and x = 385 mm has a certain degree of mutation. Through the comparative analysis of sections ‘3-3’, ‘4-4’, ‘5-5’ and ‘6-6’, it is found that the tensile stress has been reduced to a greater extent in turn, with the tensile stress value in section ‘6-6’ close to 0 at x = 90 mm to 340 mm, indicating that most of the tensile stress is not transmitted through the cover plate into the column wall, but through the cover plate to the bolt hole, and from the bolt to the angle steel. By analyzing the tensile stress values in the six sections in the figure, a significant decrease in the tensile stress values of sections ‘4-4’ and ‘5-5’ is observed, indicating that most of the tensile stress is transmitted to the bolts in the second and third rows. In addition, there are negative values of tensile stress in sections ‘4-4’, ‘5-5’ and ‘6-6’, which are caused by the friction between the surface of the nuts and the surface of the cover plates.

3.1.3. Horizontal stress distribution of angle steel

From the transmission path of the principal stress at the angle steel in Fig. 5(c), the stress transmitted from the cover plate continues to be transmitted mainly along the horizontal limb of the angle steel and finally to the steel tube.

According to the Fig. 6(c), the distribution of tensile stress on the horizontal and vertical limbs of the angle steel was analyzed respectively. Comparing the changes in stress value on the horizontal limb sections ‘1-1’ to ‘4-4’ of the angle steel, it can be seen that the closer the position of the section is to the column wall, the lower the maximum stress value of that section. In addition, the location where the stress value appears to decrease is between x = 214.3 mm and 233.4 mm. In contrast, there is a significant increase in stress in section ‘5-5’ of the angle steel’s vertical limb in this region, indicating that most of the tensile stress on the horizontal limb is transferred to the vertical limb of the angle steel. At the location where the angle steel is connected to the steel tube, i.e., x = 260 mm, there is a substantial decrease in the stress on sections ‘4-4’ and ‘5-5’, indicating that most of the tensile stress on the angle steel is eventually transferred to the wall of the steel tube.

3.1.4. Horizontal stress distribution of steel tube

From the transmission path of the principal stress in Fig. 5(d), it can be verified that most of the horizontal stress on the angle steel is introduced into the corner of the steel tube wall.

Fig. 6(d) displays the stress distribution on the composite column's steel tube. It is observed that the stress at the steel tube wall increases gradually in the range of x = 0 mm to 12 mm, indicating that most of the tensile stress on the angle steel is transferred to the steel tube in this region. Notably, the compressive stress developed on the steel tube wall in sections ‘3-3’ and ‘4-4’ is due to The angle steel being subjected to vertical shear force from the beam end thus producing bending moments near the steel tube. Similar to the bending moment at the beam end, this bending moment is also transformed into a set of forces of equal magnitude and opposite direction applied to the cross-section of the angle steel.

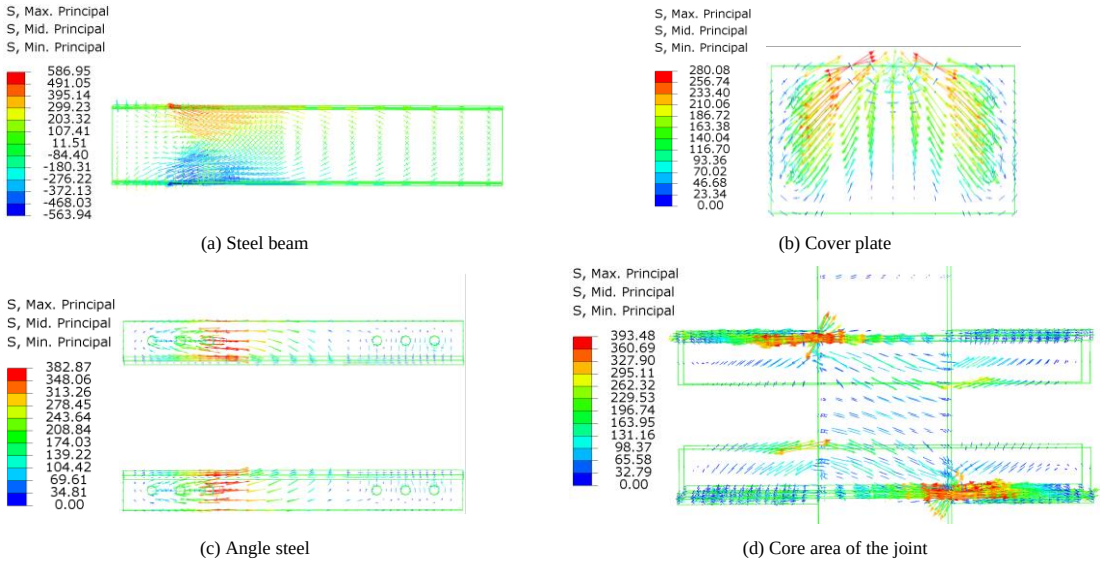

(a) Steel beam (b) Cover plate

(c) Angle steel (d) Core area of the joint

Fig. 5 The transmission path of principal stress on each component of the joint

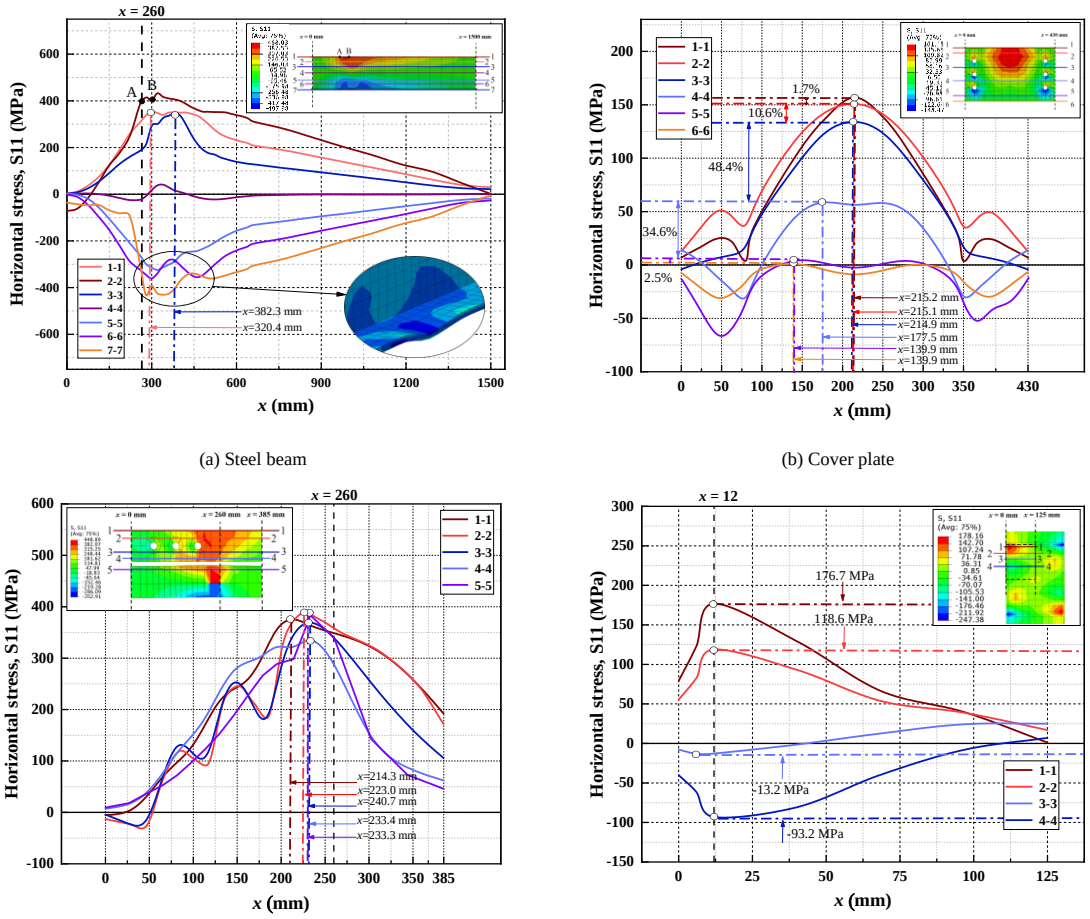

(a) Steel beam (b) Cover plate

(c) Angle steel (d) Steel tube web

Fig. 6 Horizontal stress distribution on each component of the joint

3.2. Vertical shear stress distribution

3.2.1. Vertical shear stress distribution of steel beam

The vertical stress in different sections of the steel beam was extracted using the path analysis method as shown in Fig. 7(a). There is a more obvious rise at x = 700 mm to 1500 mm in section '3-3' compared to the other sections in the figure, indicating that the shear stress at the end of the beam is delivered inward from the center of the beam web. The vertical stress of sections '2-2' and '4-4' increases in the range of x = 260 mm to 450 mm. However, the vertical stress of sections '1-1' and '5-5' only increases in the range of x = 0 mm to 260 mm, and the increase is remarkable, indicating that the shear stress began to spread to the upper and lower sides of the web at about x = 450 mm, and rapidly transferred to the upper and lower edges of the web at x = 260 mm.

3.2.2. Vertical shear stress distribution of cover plate

The vertical stress at different sections on the cover plate was analyzed as shown in Fig. 7(b). Section '1-1' shows a large vertical stress at x = 215 mm with a value of 17.2 MPa, indicating that a part of the vertical shear stress on the beam web is transferred to the centerline of the cover plate. On the other hand, section '2-2' shows a significant decrease in the vertical stress value at x = 215 mm, indicating that most of the vertical stress on the cover plate is not transferred along the centerline of the cover plate, but to the sides. It is worth noting that there is a large increase in the vertical stress at x = 80 mm to 175 mm and x = 290 mm to 350 mm for all sections, which is due to the vertical

limbs of the angle steel acting as vertical supports and providing larger reaction forces, indicating that most of the vertical shear stress on the cover plate is transferred to the vertical limbs of the angle steel. Sections '2-2', '3-3' and '4-4') show larger vertical stress at x = 45 mm and x = 395 mm, which is caused by the nut restraining the edge of the cover plate from buckling, indicating that a portion of the vertical shear stress on the cover plate is also transferred to the horizontal limbs of the angle steel through the bolts.

3.2.3. Vertical shear stress distribution of angle steel

Fig. 7(c) shows the distribution of vertical stress at different sections of the angle steel. Large vertical stress appears at x = 65 mm, x = 130 mm, and x = 195 mm for sections '1-1', '2-2' and '3-3' of the horizontal limb of the angle steel, indicating that part of the shear stress is transferred to the horizontal limb of the cover plate through the bolts. On the contrary, sections '4-4' and '5-5' show a gradual increase in vertical stress in the range of x = 0 mm to 195 mm, and the vertical stress value in section '5-5' is much higher than in other sections, indicating that most of the shear stress is transmitted into the vertical limb of the angle steel. In the range of x = 200 mm to 260 mm, the vertical stress values of sections '1-1', '2-2' and '3-3' show a substantial decrease, whereas the vertical stress values of sections '4-4' and '5-5' show a greater degree of elevation, demonstrating that the shear stress on the angle steel is transferred to the position close to the column section. Because of the restraining effect of the steel tube web on the angle steel, the maximum value of vertical stress occurs in sections '4-4' and '5-5' both at x = 360 mm, indicating that the shear stress on the sections of the angle steel is transmitted into the steel tube web.

3.2.4. Vertical shear stress distribution of steel tube

The shear stress distribution on different sections of the steel tube wall is shown in Fig. 7(d). The vertical stress values at y = 112.5 mm and y = 412.5 mm for section '1-1' are 495.6 MPa and 158.4 MPa respectively, indicating that a part of the vertical stress on the beam web is directly transferred to the steel tube wall. About 70% of the vertical shear stress is transmitted to the steel tube along the web on the compressed side of the steel beam. The vertical shear stress of sections '2-2' and '3-3' at y = 112.5 mm is increased by 6.7 % and 9.1 % respectively, with a minor increase in stress values. In contrast, the vertical stress values at y = 412.5 mm in both sections show a significant change, indicating that there is also a portion of vertical shear stress transmitted into the corner of the steel tube wall through the angle steel, and mainly through the angle steel on the tensile side.

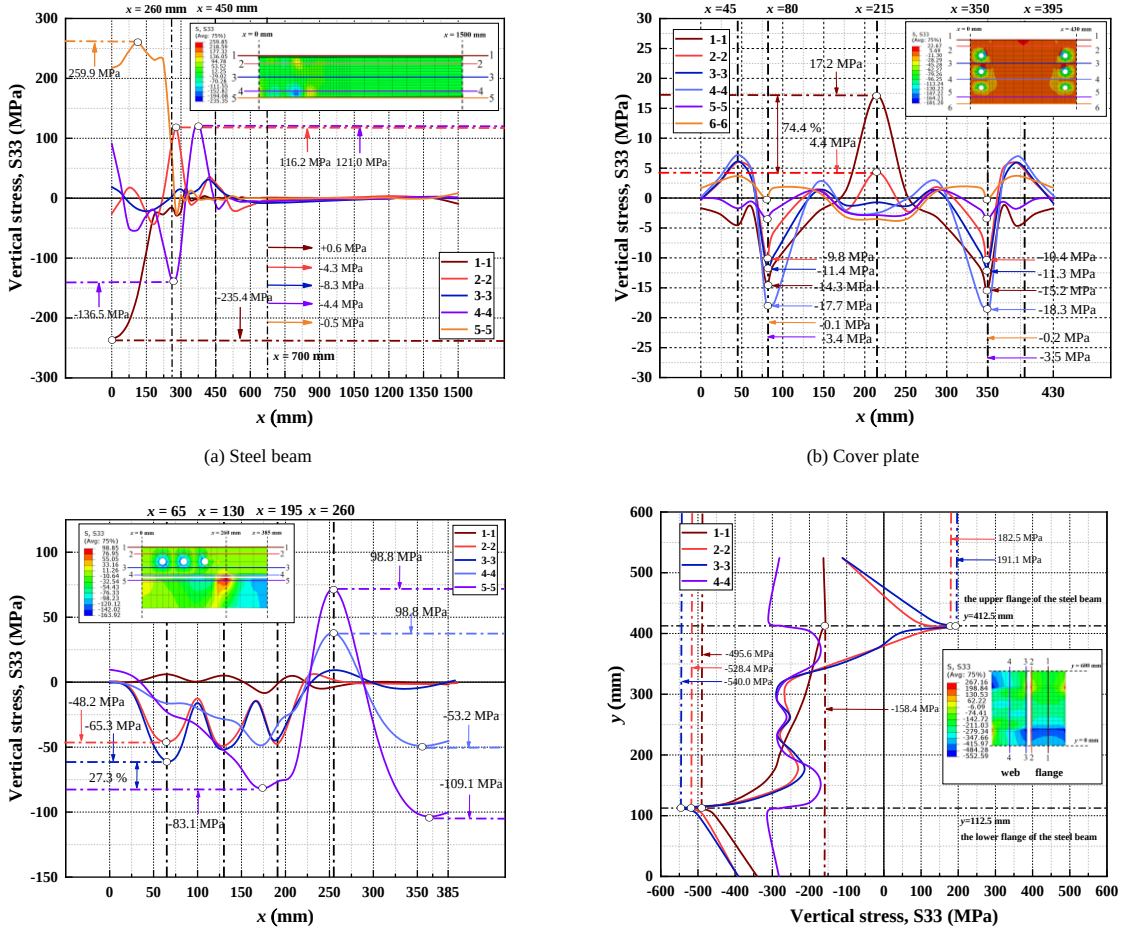

(a) Steel beam (b) Cover plate

(c) Angle steel (d) Steel tube

Fig. 7 Vertical stress distribution on each component of the joint

3.3. Stress distribution in the panel zone of the combined column

Considering the previous analysis, it is clear that the horizontal force acting on the beam flange and the vertical shear force acting on the beam web is eventually introduced into the column wall through the components of the joint. As a result, the horizontal forces and vertical shear force from the beam end are transformed into shear force after being transferred into the panel zone of the combined column. Fig. 8 shows the stress distribution within the core area of the joint is shown in Fig. 8. It has been noted that the steel tube web, the infilled concrete, and the I-shaped CFRP profile web all take the shear force within the joint's core area. Among them, the shear force shared by the steel tube web is significantly greater than the shear force shared by the concrete and CFRP profiles.

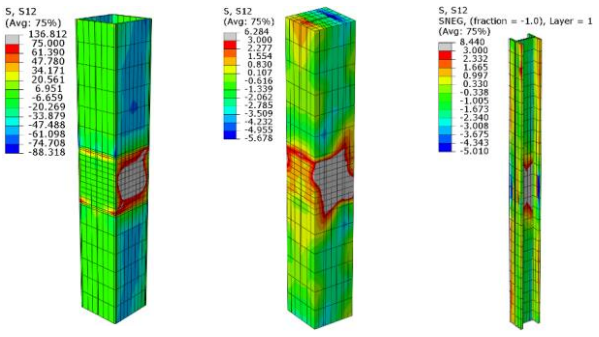

(a) Square steel tube (b) Infilled concrete (c) I-shaped CFRP profile

Fig. 8 Shear stress distribution in the panel zone

3.4. Transmission path of the joint

In summary, the transmission paths of the horizontal and shear forces on the beam are shown in Table 2. In addition, a single diagram to demonstrate the transmission path schematic of the external cover plate joint is shown in Fig. 9. In this diagram, *M* represents the bending moment supplied to the beam section, *N* represents the compressive load transferred along the beam flange, *T* represents the tensile load sent along the beam flange, and *V* represents the shear force transmitted along the beam web.

Table 2
The transmission path of the joint

Horizontal force	Beam flange → Cover plate → Angle steel → Steel tube
Vertical shear force	Beam web → Steel tube
	Beam web → Cover plate → Angle steel → Steel tube

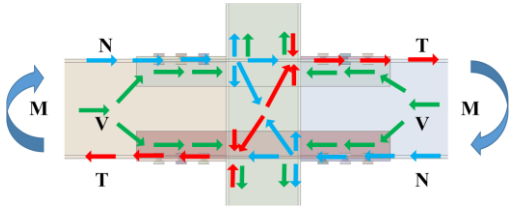

Fig. 9 Schematic diagram of the transmission path

4. Initial rotational stiffness analysis

The component analysis is a method currently used by the Eurocode to determine the initial rotational stiffness of beam-column joints. According to the concept of the component method, any joint can be divided into three different parts: tensile, compressive, and shear regions. Each region has several load-bearing components to bear the corresponding load. According to the analysis of the load transfer mechanism in Section 3, it is clear that the transmission mechanism of this joint is simple, and all components are planar components, so this new combined joint can be analyzed by applying the principle of the component method.

A crucial factor in describing the moment-rotation curve is the initial rotational stiffness. To obtain its precise formula, we simplified the basic components of the joint to spring elements based on the principles of component analysis. First, we calculated the stiffness of each spring element, and then we combined all spring elements into a simplified spring model. Finally, the initial rotational stiffness of the entire joint was calculated.

4.1. The basic components of the joint

The joint can be divided into tensile, compressive and shear regions under loading, and each part consists of several components. These components can simplify the two-dimensional force model of the joint under bending moment to the one-dimensional force model under tension and compression for calculation.

By analyzing the load transfer mechanism of the joint, the tensile (compressive) components are mainly the steel tube web, cover plate, angle steel, steel beam flange, and steel beam web; the shear components are mainly the steel tube web, concrete and I-shaped CFRP profile web.

4.2. Simplified spring model

The following can be assumed in light of the finite element analysis's findings: (1) Each member is in an elastic condition, and there is only minor deformation; (2) Each component satisfies the plane section assumption; (3) The center of rotation is centered between the flanges on either side of the beam.

The connecting portion of the entire joint is simulated by five pairs of springs, namely the cover plate, angle steel, beam flange, beam web, and the steel tube web in bending. The core area of the joint is simulated by three springs, namely the steel tube web in shear, the concrete in shear and the I-shaped CFRP profile web in shear. By dividing the tensile and compressive stress regions at the beam web (Fig. 10), the joint is simplified to a set of springs, and thus the rotation resulting from the bending deformation of the steel beam web is considered.

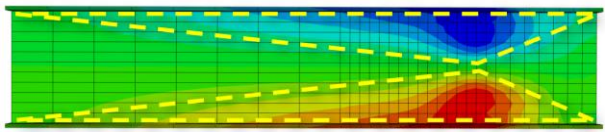

Fig. 10 Division of stress region

In calculating the rotation caused by the lateral deformation of the column section subjected to shear, the shear deformation of each component in the composite column can be considered the same due to the cooperative working characteristic of the column. Therefore, the steel tube web, concrete and I-shaped CFRP profile web can be modeled as three parallel shear springs. In summary, the joint is simplified to the spring element model in Fig. 11(a). After unifying the springs with the same force state, an equivalent spring element model can be obtained (Fig. 11(b)).

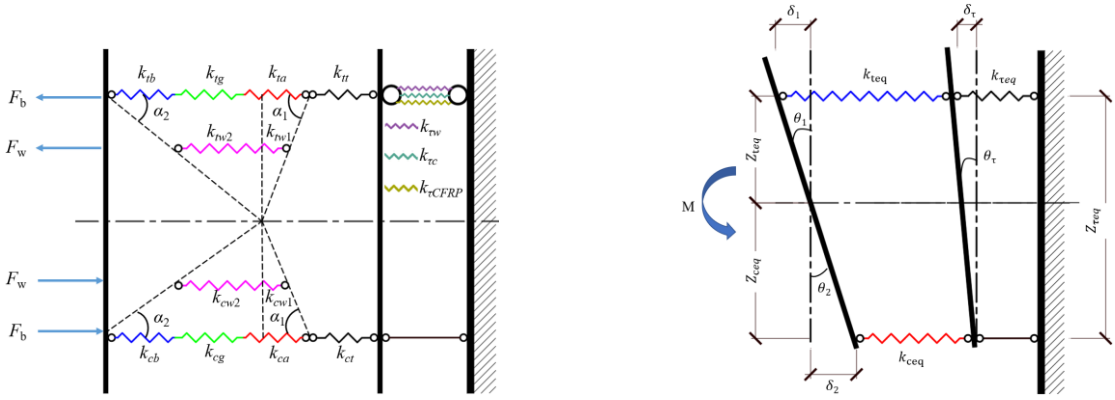

(a) Spring element model (b) Equivalent spring element model

Fig. 11 Calculation model for initial stiffness

In Fig. 11, k_{tb} and k_{cb} stand for the stiffness of beam flange under tension and compression respectively. k_{tg} and k_{cg} represent the stiffness of the cover plate under tension and compression. k_{ta} and k_{ca} are the stiffness of angle steel under tension and compression. k_{tt} and k_{ct} are the stiffness of steel tube web under tension and compression. k_{tw} for the tensile stiffness of the steel beam web, which is divided into two portions, k_{tw1} and k_{tw2}. k_{cw} stands for the compressive stiffness of the steel beam web, including k_{cw1} and k_{cw2}. $k_{\tau w}$ stand for the shear stiffness of the steel tube web, $k_{\tau c}$ represents the shear stiffness of the concrete, and $k_{\tau CFRP}$ means the shear stiffness of the I-shaped CFRP profile web. k_{teq}, k_{ceq} and $k_{\tau eq}$ denote the equivalent stiffness of the joint under tension, compression and shear respectively. δ_1 stands for tension-related deformation, δ_2 for compression-related deformation, and δ_τ for shear-related deformation. θ_1 is the rotation caused by tensile deformation, θ_2 is the rotation caused by compressive deformation, and θ_τ is the rotation caused by shear deformation. Z_{teq} represents the equivalent distance between the centroid of the tension spring element and the beam centre, Z_{ceq} stands for the equivalent distance between the centroid of the compression spring element and the beam centre, and Z_{teq} for the equivalent height of shear section.

Corresponding to Fig. 11, the following equations are established according to the force equivalence and bending distance equivalence:

$$k_{teq}Z_{teq}\theta_1 = k_{tg}Z_{tg}\theta_1 + k_{tb}Z_{tb}\theta_1 + k_{tw1}Z_{tw}\theta_1 + k_{tw2}Z_{tw}\theta_1 + k_{ta}Z_{ta}\theta_1 + k_{tt}Z_{tt}\theta_1 \quad (1)$$

$$k_{teq}Z_{teq}^2\theta_1 = k_{tg}Z_{tg}^2\theta_1 + k_{tb}Z_{tb}^2\theta_1 + k_{tw1}Z_{tw}^2\theta_1 + k_{tw2}Z_{tw}^2\theta_1 + k_{ta}Z_{ta}^2\theta_1 + k_{tt}Z_{tt}^2\theta_1 \quad (2)$$

$$k_{ceq}Z_{ceq}\theta_2 = k_{cg}Z_{cg}\theta_2 + k_{cb}Z_{cb}\theta_2 + k_{cw1}Z_{cw}\theta_2 + k_{cw2}Z_{cw}\theta_2 + k_{ca}Z_{ca}\theta_2 + k_{ct}Z_{ct}\theta_2 \quad (3)$$

$$k_{ceq}Z_{ceq}^2\theta_2 = k_{cg}Z_{cg}^2\theta_2 + k_{cb}Z_{cb}^2\theta_2 + k_{cw1}Z_{cw}^2\theta_2 + k_{cw2}Z_{cw}^2\theta_2 + k_{ca}Z_{ca}^2\theta_2 + k_{ct}Z_{ct}^2\theta_2 \quad (4)$$

Combining Eqs. (1 to 4) yields:

$$Z_{teq} = \frac{k_{tg}Z_{tg}^2 + k_{tb}Z_{tb}^2 + k_{tw1}Z_{tw}^2 + k_{tw2}Z_{tw}^2 + k_{ta}Z_{ta}^2 + k_{tt}Z_{tt}^2}{k_{tg}Z_{tg} + k_{tb}Z_{tb} + k_{tw1}Z_{tw} + k_{tw2}Z_{tw} + k_{ta}Z_{ta} + k_{tt}Z_{tt}} \quad (5)$$

$$Z_{ceq} = \frac{k_{cg}Z_{cg}^2 + k_{cb}Z_{cb}^2 + k_{cw1}Z_{cw}^2 + k_{cw2}Z_{cw}^2 + k_{ca}Z_{ca}^2 + k_{ct}Z_{ct}^2}{k_{cg}Z_{cg} + k_{cb}Z_{cb} + k_{cw1}Z_{cw} + k_{cw2}Z_{cw} + k_{ca}Z_{ca} + k_{ct}Z_{ct}} \quad (6)$$

$$k_{teq} = \frac{(k_{tg}Z_{tg} + k_{tb}Z_{tb} + k_{tw1}Z_{tw} + k_{tw2}Z_{tw} + k_{ta}Z_{ta} + k_{tt}Z_{tt})^2}{k_{tg}Z_{tg}^2 + k_{tb}Z_{tb}^2 + k_{tw1}Z_{tw}^2 + k_{tw2}Z_{tw}^2 + k_{ta}Z_{ta}^2 + k_{tt}Z_{tt}^2} \quad (7)$$

$$k_{ceq} = \frac{(k_{cg}Z_{cg} + k_{cb}Z_{cb} + k_{cw1}Z_{cw} + k_{cw2}Z_{cw} + k_{ca}Z_{ca} + k_{ct}Z_{ct})^2}{k_{cg}Z_{cg}^2 + k_{cb}Z_{cb}^2 + k_{cw1}Z_{cw}^2 + k_{cw2}Z_{cw}^2 + k_{ca}Z_{ca}^2 + k_{ct}Z_{ct}^2} \quad (8)$$

where Z_{tg} and Z_{cg} are the distance between the centroid of the spring element of the cover plate and the beam center, Z_{tb} and Z_{cb} are the distance between the centroid of the spring element of the steel beam flange and the beam center, Z_{tw} and Z_{cw} are the distance between the centroid of the spring element of the steel beam web and the beam center, Z_{ta} and Z_{ca} are the distance between the centroid of the spring element of the angle steel and the beam center, and Z_{tt} and Z_{ct} are the distance between the centroid of the spring element of the steel tube web and the beam center.

Under pure bending, the calculation models of tensile and compressive stiffness are the same, the areas of joints under tension and compression are symmetrical, and the tensile stiffness is the same as the compressive stiffness. Thus, $Z_{teq}= Z_{ceq}$; $k_{teq}= k_{ceq}$.

The shear deformation δ_τ in the core zone of the joint is mainly contributed by the web of square steel tube ($\delta_{\tau w}$), the cross-section of the infilled concrete ($\delta_{\tau c}$) and the cross-section of the I-shaped CFRP profile web ($\delta_{\tau CFRP}$). The force and deformation of each shear spring satisfy the relationship as follows:

$$F_s = F_{\tau w} + F_{\tau c} + F_{\tau CFRP} \quad (9)$$

$$\delta_\tau = \delta_{\tau\omega} = \delta_{\tau c} = \delta_{\tau CFRP} \quad (10)$$

where F_s is the total shear assumed by the core zone of the joint, $F_{\tau w}$, $F_{\tau c}$ and $F_{\tau CFRP}$ are the shear force taken by the steel tube, the infilled concrete, and the I-shaped CFRP profile web, respectively.

The following equation is established according to the cooperative working characteristic of the column:

$$k_{\tau eq} = k_{\tau\omega} + k_{\tau c} + k_{\tau CFRP} \quad (11)$$

4.3. Calculation of the mechanical model of the plate

Fig. 12 shows the mechanical calculation model of the plate. Based on Hooke's law of a tension rod, the tensile stiffness of the rectangular plate (Fig. 12(a)) is calculated according to Eqs. (12 to 15); while the tensile stiffness of the triangular plate (Fig. 12(b)) is calculated by Eq. (16).

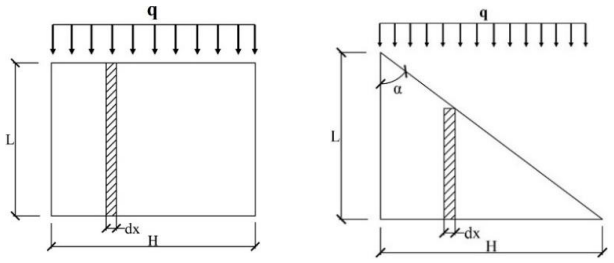

(a) Rectangular plate (b) Triangular plate

Fig. 12 Mechanical model of the panel

Adopting the calculation method in reference [29], the tensile stiffness in Eq. (15) of the rectangular plate can be derived according to Eqs. (12 to 14),

$$A = \int_0^H t dx = Ht \quad (12)$$

$$\Delta L = \frac{FL}{EA} = \frac{FL}{EHt} \quad (13)$$

$$k = \frac{F}{\Delta L} \quad (14)$$

$$k_R = \frac{EHt}{L} \quad (15)$$

similarly, the tensile stiffness of the triangular plate is calculated as:

$$k_T = Et \cdot \tan\alpha \quad (16)$$

In Eqs. (12 to 16), ΔL is the deformation of the panel induced by the force. F is the tensile force on the panel. A is the area of the panel. L and H are the lengths of the panel in the direction of force and vertically to the direction of force respectively. E and t stand for the elastic modulus and thickness of the panel respectively. k, k_R and k_T are the stiffness namely the general panel under tension, the rectangular panel under tension and the triangular panel under tension, respectively.

4.4. Calculation of the initial rotational stiffness

4.4.1. Calculation of the component stiffness under tension (compression)

Based on Fig. 12 and Eqs. (15 and 16), the stiffness of each spring element can be calculated as follows:

$$k_{tg} = \frac{E_g l_g t_g}{b_g} \quad (17)$$

$$k_{tb} = \frac{E_b b_f t_f}{l_b} \quad (18)$$

$$k_{tw1} = \frac{E_w t(h_b - 2t_f)}{2b_g} \quad (19)$$

$$k_{tw2} = \frac{E_w t(h_b - 2t_f)}{2(l_b - b_g)} \quad (20)$$

$$k_{ta} = \frac{E_a b_a t_a}{l_a} \quad (21)$$

$$k_{tt} = \frac{E_t(h_a + 2t_g)t_t}{2l_t} \tag{22}$$

In Eqs. (17 to 22), E_g, E_b, E_w, E_a and E_t are the elastic modulus of components namely cover plate, steel beam flange, steel beam web, angle steel and steel tube web, respectively. l_g, l_a, l_t and l_b are the lengths of the components namely cover plate, angle steel, square steel tube and steel beam, separately. The thickness of the cover plate, angle steel, square steel tube and steel beam flange applies t_g, t_a, t_t and t_f to represent in the above formulas. b_a and b_g are the width of the angle steel limb and cover plate along the beam. h_b represents the height the of steel beam section.

According to the structure of the external cover plate joint, the rotational distance between each spring element and the beam center is calculated as follows :

$$Z_{tg} = \frac{h_b + t_g}{2} \tag{23}$$

$$Z_{tb} = \frac{h_b - t_f}{2} \tag{24}$$

$$Z_{tw} = \frac{h_b - 2t_f}{3} \tag{25}$$

$$Z_{ta} = \frac{h_b - t_a}{2} \tag{26}$$

$$Z_{tt} = \frac{h_b + 2t_g}{4} \tag{27}$$

Substituting the stiffness and rotational distance of each component into Eqs. (5 to 8) yields k_{teq}, k_{ceq}, Z_{teq}, and Z_{ceq}.

4.4.2. Calculation of shear component stiffness

The above analysis shows that the shear force is mainly supported by the steel tube, concrete and CFRP profile web in the panel zone of the joint. In order to determine its stiffness in shear ($\delta_{cw,v}$), the panel zone of the joint can be viewed in Fig. 13 as a short column subjected to shear [16]. As a result, Eq. (28) can be used to determine the shear deformation of the column web under shear.

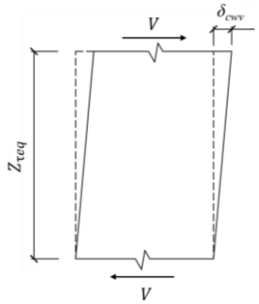

Fig. 13 Deformation of the column web under the shear force

$$\delta_{cw,v} = \frac{VZ_{teq}}{GA_{v,cw}} \tag{28}$$

where $A_{v,cw}$ stands for the shear cross-sectional area of the column web.

The shear force on the column web can be obtained from the horizontal force transmitted from the beam flange as in Eq. (29).

$$V = \beta F_{t,bf} \tag{29}$$

where β is the parameter related to the number of sheared edges. Since the object of this paper belongs to the beam-column joint of the middle column, and the bending moment applied on both sides of the joint has equal value and the same direction, β can be taken as 2 [30].

Utilizing the previous mentioned formula, the shear deformation of steel tube web ($\delta_{\tau w}$), the shear deformation of concrete ($\delta_{\tau c}$), and the shear deformation of I-shaped CFRP profile web ($\delta_{\tau CFRP}$) are derived as follows:

$$\delta_{\tau w} = 2(1+\nu)\frac{VZ_{teq}}{E_t A_{\tau w}} \tag{30}$$

$$\delta_{\tau c} = \frac{VZ_{teq}}{G_{\tau c}[(l_t - 2t_t)^2 - A_{CFRP}]} \tag{31}$$

$$\delta_{\tau w,CFRP} = \frac{VZ_{teq}}{G_{\tau CFRP}A_{\tau CFRP}} \tag{32}$$

In Eqs. (30 to 32), $G_{\tau c}$ and $G_{\tau CFRP}$ represent the shear modulus of concrete and I-shaped CFRP profile web, respectively. $A_{\tau w}$, $A_{\tau c}$, and $A_{\tau CFRP}$ are the shear cross-sectional area namely steel tube web, infilled concrete and I-shaped CFRP profile web. ν represents the Poisson's ratio.

Substituting the above parameters into Eq. (14) yields the stiffness of each shear component as follows:

$$k_{tw} = \frac{F_{tw}}{\delta_{\tau w}} = \frac{E_w l_t t_t}{2(1+\nu)\beta Z_{teq}} \tag{33}$$

$$k_{\tau c} = \frac{F_{\tau c}}{\delta_{\tau c}} = \frac{G_{\tau c}[(l_t - 2t_t)^2 - A_{CFRP}]}{\beta Z_{teq}} \tag{34}$$

$$k_{\tau w,CFRP} = \frac{F_{\tau CFRP}}{\delta_{\tau CFRP}} = \frac{G_{\tau w,CFRP}A_{\tau w,CFRP}}{\beta Z_{teq}} \tag{35}$$

From Eq. (10), the equivalent shear stiffness can be yielded as follows:

$$k_{\tau eq} = \frac{E_w l_t t_t}{2(1+\nu)\beta Z_{teq}} + \frac{G_{\tau c}[(l_t - 2t_t)^2 - A_{CFRP}]}{\beta Z_{teq}} + \frac{G_{\tau w,CFRP}A_{\tau w,CFRP}}{\beta Z_{teq}} \tag{36}$$

where $Z_{\tau eq} = h_b + 2t_g$.

4.4.3. Calculation of initial rotational stiffness of the whole joint

The rotations caused by moment deformation and shear deformation under the application of external load are calculated as follows:

$$\delta_c = \frac{M}{Z_{eq}k_{ceq}} \tag{37}$$

$$\delta_t = \frac{M}{Z_{eq}k_{teq}} \tag{38}$$

$$\delta_\tau = \frac{M}{Z_{\tau eq}k_{\tau eq}} \tag{39}$$

The joint's overall rotation (θ) can be separated into the rotation (θ_M) caused by bending deformation and the rotation (θ_τ) brought on by shear deformation, so the rotation of the joint satisfies Eq. (40). The bending moment at the end of the beam is transformed into a set of the horizontal force of tension and compression at the upper and lower flanges, and the rotation caused by the bending moment can be separated into the rotation (θ_1) caused by tensile deformation and the rotation (θ_2) caused by compressive deformation of the component, as shown in Eq. (41).

$$\theta = \theta_M + \theta_\tau \tag{40}$$

$$\theta_M = \theta_1 + \theta_2 \tag{41}$$

Substituting Eqs. (37 to 39) into Eqs. (40 and 41), the rotation caused by the overall deformation of the joint can be yielded as follows:

$$\theta = \theta_M + \theta_\tau = \frac{\delta_t + \delta_c}{Z_{eq}} + \frac{\delta_\tau}{Z_{\tau eq}} = M[\frac{1}{Z_{eq}^2}(\frac{1}{k_{teq}} + \frac{1}{k_{ceq}}) + \frac{1}{Z_{\tau eq}^2 k_{\tau eq}}] \tag{42}$$

Finally, the initial rotational stiffness (K_i) can be calculated as follows :

$$K_i = \frac{M}{\theta} = \frac{1}{\frac{1}{Z_{eq}^2}(\frac{1}{k_{teq}} + \frac{1}{k_{ceq}}) + \frac{1}{Z_{\tau eq}^2 k_{\tau eq}}} = \frac{1}{\frac{2}{Z_{eq}^2 k_{teq}} + \frac{1}{Z_{\tau eq}^2 k_{\tau eq}}} \tag{43}$$

4.4.4. Verification of the calculation results for initial rotational stiffness

Currently, the initial rotational stiffness of the joint is defined mainly through two methods, as shown in Fig. 14. The first is the initial stiffness defined by the first-order derivative of the moment-rotation curve of the joint at the origin, as shown in Eq. (44).

$$K_0 = \left.\frac{dM}{d\theta}\right|_{\theta=0} \tag{44}$$

The second one is defined by the secant stiffness (K_s) of the line between the data point and the origin corresponding to a certain percentage of the characteristic load on the moment-rotation curve of the joint. Usually, K_0 will be higher than the actual stiffness of the joint when the load is larger, and the larger the load, the larger the deviation. Therefore, many scholars mostly use the secant stiffness (K_s) in the moment-rotation model to define the initial stiffness in practical applications. In this paper, the initial stiffness is taken with reference to the method of Han [24] for the stiffness of purely bending members, and the secant stiffness corresponding to 0.2 M_u on the moment-rotation curve is taken as the initial rotational stiffness of the joint, so α is taken as 0.2.

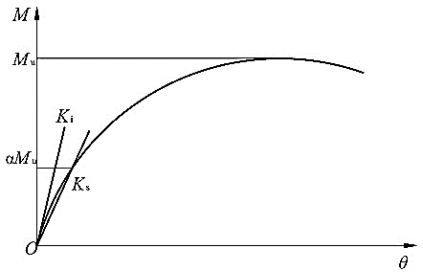

Fig. 14 Definition of initial stiffness

The finite element analysis of joints with various cover plate widths and thicknesses under monotonic static load is carried out by ABAQUS. Comparing the results of initial rotational stiffness calculated by the theoretical calculation model and finite element simulation in Table 3, it is clear that the mean of the ratio between theoretical calculation values and finite element analysis results is 0.91, and the standard deviation is 0.09. The above results demonstrate that the initial rotational stiffness calculated by the model agrees well with finite element analysis ones.

Table 3
Verification results of initial rotational stiffness

Model	Cover plate width /mm	Cover plate thickness /mm	Theoretical calculation result k_1/ kN·m·rad^{-1}	Finite element analysis k_2/ kN·m·rad^{-1}	k_1/ k_2
BK200	200	10	20743.86	25089.27	0.83
BK260	260	10	18617.68	23388.58	0.80
BK320	320	10	15347.74	15542.21	0.99
BH8	260	8	16150.10	15697.73	1.03
BH12	260	12	21626.79	24527.59	0.88
BH15	260	15	25496.74	27467.17	0.93
Average					0.91
Standard deviation					0.09

5. Calculation of ultimate bending moment

Because the joint's bending capacity is determined by the load-bearing ability of the failing component, which is typically the component with the lowest load-bearing capacity. In summary, it is necessary to analyze the possible failure modes of the external cover plate joint to calculate the flexural bearing capacity.

The possible failure modes of the joint are simulated by finite elements as shown in Fig. 15. The CFSST column is not damaged under lateral compression and shear in the core area. Therefore, the above two failure modes are not considered when calculating the ultimate bending moment of the joint to facilitate the practical engineering application, and only the following three possible failure modes are considered:

1) failure at the plastic hinge of beam section;
2) failure at the end of the cover plate connected to the steel tube;
3) failure at the angle steel section.

The ultimate capacity of various components of the joint under each of the above failure modes is calculated, thereby obtaining the ultimate flexural resistance of the joint.

It is worth noting that the finite element models used to analyze the failure modes all use the materials specified in Table 1. Therefore, the formula of ultimate bending moment obtained by the above method is only applicable to the joint using the materials in Table 1.

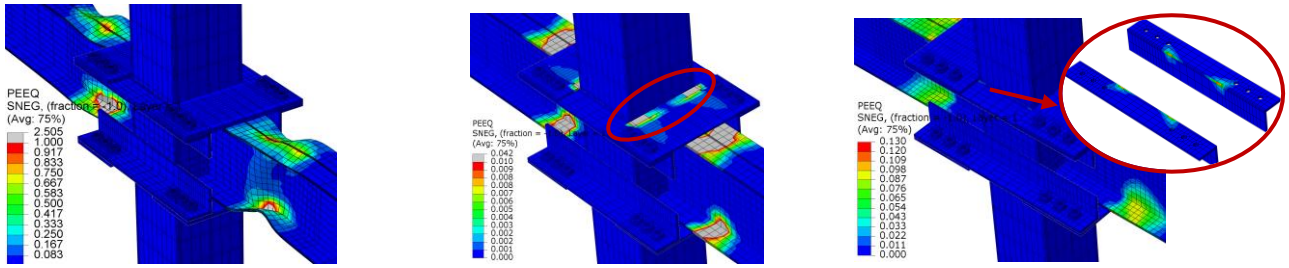

(a) Failure at the plastic hinge of beam section (b) Failure at the cover plate (c) Failure at the angle steel

Fig. 15 Failure models of the joint

5.1. Failure at the plastic hinge of beam section

Refering to Fig. 16, the plastic hinge of the beam section is assumed to be located approximately at the end of the cover plate. When the beam section appears a plastic hinge, the ultimate bending moment of the joint should be calculated by a similar triangular relationship considering the distance between the plastic hinge section and the column face.

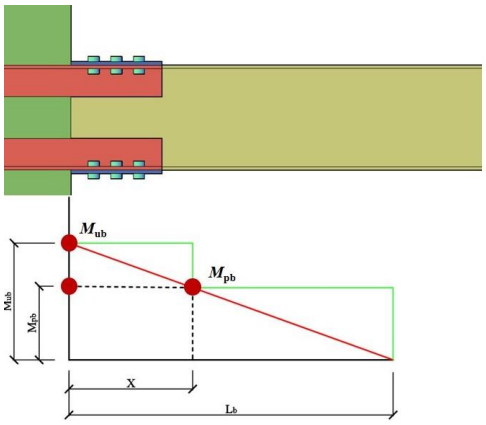

Fig. 16 Diagram of the bending capacity of the joint

Eqs. (45 and 46) can be used to determine the ultimate bending moment if damage happens to the steel beam's plastic hinge section as a result of the analysis above.

$$M_{ub} = \frac{M_{pb} L_b}{L_b - x} \tag{45}$$

$$M_{pb} = W_{pn} f_y \tag{46}$$

where M_{ub} stands for the ultimate bending moment of the joint, M_{pb} represents the ultimate bending moment of the section where the beam plastic hinge is located. In Eq. (45), L_b denotes the distance between the position of the load applied to the beam and the column wall, x is the distance of the plastic hinge position from the column wall. In Eq. (46), the plastic section modulus of the beam adopted W_{pn} to represent, and f_y is the yield strength of the steel.

The plastic resistance moment of the beam section is calculated as follows :

$$W_{pn} = 2S_n = 2\left[\frac{t_f b_f (h_b - t_f)}{2} + \frac{t_w (h_b - 2t_f)^2}{8}\right] \tag{47}$$

where S_n denotes the area moment from half of the beam section to the neutral axis of the plastic hinge, t_w is the thickness of the beam web, and b_f is the width of the beam flange.

The plastic ultimate bending moment of the steel beam is calculated according to the following formula：

$$M_{pb} = W_{pn} f_y = \left[t_f b_f (h_b - t_f) + \frac{t_w (h_b - 2t_f)^2}{4}\right] f_y \tag{48}$$

Substituting Eq. (48) into Eq. (45), the ultimate bending moment (M_{ub}) of the joint is obtained when the plastic hinge section of the steel beam is damaged.

5.2. Failure at the cover plate

Referring to the calculation method of the bending resistance of the through-diaphragm joint [31], the bending resistance of the joint mainly depends on the tensile capacity of the diaphragm, as shown in Fig. 17. The bending capacity of the joint can be obtained by multiplying the tensile capacity of the diaphragm by the center distance of the diaphragms. The formula for calculating the bending capacity is shown as follows:

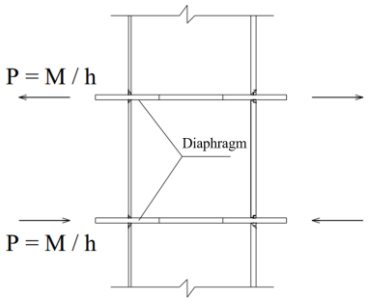

Fig. 17 Matsui calculation model

$$M = Ph = P(h_b - t_{bf}) \tag{49}$$

where P is the tensile capacity of the diaphragm, h is the center distance of the diaphragm, h_b denotes the height of the beam section, and t_{bf} represents the thickness of the beam flange.

Through the analysis of the horizontal force transmission mechanism in Section 3, it is known that the cover plate is subjected to the horizontal force transmitted by the flange of the steel beam. The tensile yielding capacity at the cross-section of the cover plate can be expressed as follows:

$$P_y^g = f_y^g A_g = f_y^g t_g l_g \tag{50}$$

In Eq. (50), P_y^g represents the yield capacity of the cover plate under tensile force, which can be derived by multiplying the yield strength of the steel applied for cover plate f_y^g by the cross-sectional area of the cover plate A_g. Where A_g can be obtained by multiplying the effective length of the cover plate l_g by the thickness of the cover plate t_g and then by f_y^g.

The ultimate tensile capacity of the cover plate can be obtained by substituting its yield strength with the ultimate strength of the steel plate used for the cover plate, and the ultimate bending capacity of the joint can be obtained by multiplying the ultimate tensile capacity of the cover plate by the center distance between the upper and lower cover plates as follows:

$$M_{ug} = P_u^g h_g = f_g^u t_g l_g h_g \tag{51}$$

where M_{ug} is the ultimate bending moment of the joint when the failure occurs at the cover plate, P_u^g is the tensile ultimate capacity of the cover plate and f_u^g denotes the ultimate strength of steel applied for cover plate.

5.3. Failure at the angle steel

From the analysis in Section 3, it is clear that the horizontal load on the cover plate is transferred to the angle steels on both sides through the bolts. Therefore, the angle steels on both sides should be considered for calculating the flexural bearing capacity of the joint. In addition, since the horizontal tension on the angle steel is transmitted not only through the horizontal limb, but also through the vertical limb, approximately the entire section of the angle steel can be considered in tension when calculating the tensile capacity of the angle steel.

In case of damage to the angle steel, the formula for determining the ultimate bending moment of the joint is provided by Eq. (52).

$$M_{ua} = 2P_u^a h_a = 2 f_u^a \left[t_a b_a + t_a (b_a - t_a)\right] h_a \tag{52}$$

where M_{ua} is the ultimate bending moment of the joint when the angle steel fails, P_u^a is the ultimate tensile capacity of the angle steel, h_a is the centroid distance between the upper and lower angle steels, f_u^a is the ultimate strength of steel for the angle steel, t_a is the thickness of the angle steel, and b_a is the width of the angle steel limb.

Through the above analysis, the ultimate bending moment under each failure mode can be obtained. Finally, the smallest ultimate bending moment is

selected as the ultimate flexural capacity of this joint, as follows:

$$M_u = \min\left\{M_{ub}; M_{ug}; M_{ua}\right\} \tag{53}$$

5.4. Verification of the calculation results for ultimate bending moment

To validate the correctness of the above method for determining the ultimate flexural capacity, adopting the proposed theoretical model and finite element simulation calculates all specimens in Table 4. From the comparison results between the above two methods, the average is 1.01, and the standard deviation is 0.02, illustrating that the ultimate flexural capacity calculated by the presented formula agrees well with the finite element simulation results, which can verify the accuracy of the formula for determining the ultimate bending moment proposed in this paper.

Table 4
Verification results of the ultimate bending moment

Model	Cover plate width /mm	Cover plate thickness /mm	Theoretical calculation result M_1/ kN·m	Finite element analysis M_2/ kN·m	M_1/M_2
BK200	200	10	230.3	233.7	0.99
BK260	260	10	241.4	235.8	1.02
BK320	320	10	253.7	245.1	1.04
BH8	260	8	230.1	231.9	0.99
BH12	260	12	241.5	236.3	1.02
BH15	260	15	241.5	236.6	1.02
Average					1.01
Standard deviation					0.02

6. Moment-rotation curve

6.1. Introduction of typical representations

The moment-rotation curve of the joint can reflect the rotation capacity and moment resistance of the joint. Therefore, exploring the mathematical expression function of the moment-rotation curve of the joint is helpful for the internal force analysis and design of the joint. At present, there are two main mathematical models for the moment-rotation curve of joints proposed by many scholars. One is the curve model defined by a piecewise function, and the other is the curve model defined by a single nonlinear function. The existing moment-rotation curve models take the moment resistance and initial rotational stiffness of the joints as the basic physical parameters. In addition, shape parameters are introduced in some curve models. In this paper, three typical curve models are introduced and compared.

6.1.1. Trilinear model

The trilinear model is regarded as the simplest model considering the mechanical behavior of the joints, which consists of the elastic, knee and ultimate components. The mathematical expression of the trilinear model in reference [13] can be expressed in Eq. (54), where $\theta_y = M_y / k_i$ is the yield rotation of the joint. To illustrate this model more clearly, the moment-rotation curves of the external cover plate joint calculated by the trilinear model are shown in Fig. 19. It is observed that the moment-rotation curves derived from the trilinear model have significant errors in the knee part compared with the finite element analysis results, which cannot accurately reflect the mechanical behavior of the joint. In addition, sharp points tend to appear at the breakpoints of the piecewise function, which may cause numerical problems such as computational non-convergence in the subsequent structural analysis.

$$M = \begin{cases} K_i\theta, & \theta \le \theta_y \\ M_y + \dfrac{K_i}{7}\left(\theta - \theta_y\right), & \theta_y < \theta \le 4.5\theta_y \\ 1.5M_y & \theta > 4.5\theta_y \end{cases} \tag{54}$$

6.1.2. Function model in Eurocode 3

As shown in Eq. (55), similar to the trilinear model, the moment-rotation model provided in Eurocode 3 is also defined by three parts, which also consists of the elastic, knee and ultimate parts [32]. However, compared with the trilinear model, the shape coefficient ζ is introduced in the knee part of this model to adjust the curve shape so that the calculation results of this model are more precise. The moment-rotation curves obtained by using the function model in Eurocode 3 are also shown in Fig. 19. Based on the results in the figure, the knee part of this model curve is more accurate than the trilinear model, but there are still obvious errors. In addition, this model only considers the continuity but not the smooth conditions at breakpoints, which may still cause numerical problems such as non-convergence in subsequent structural analysis.

$$M = \begin{cases} K_i\theta, & \theta \le \theta_y \\ (M_y^{\zeta} K_i \theta)^{\frac{1}{1+\zeta}}, & \theta_y < \theta \le 4.5\theta_y \\ 1.5M_y & \theta > 4.5\theta_y \end{cases} \tag{55}$$

6.1.3. Exponential function model

Zhao [33] proposed an exponential function model containing three main parameters, which includes shape coefficients c to adjust the curve shape. Compared with the four-parameter exponential model proposed by Yee [16], the complex process of introducing strain hardening stiffness to predict the ultimate state of joints is omitted. The model reduces the workload of calculating the moment-rotation curve while ensuring prediction accuracy. The mathematical expression of the exponential function model proposed by Zhao is shown in Eq. (56). For a clearer presentation of the model, Fig. 19 shows the moment-rotation curves of the external cover plate joint obtained by using the three-parameter exponential function model. Due to the fact that the moment-rotation curves are defined by a single nonlinear function, these curves are continuous and smooth. Therefore, numerical problems such as non-convergence can be avoided in subsequent structural analysis. However, this function model does not distinguish the elastic part of joints. As a result, when the shape coefficient is adjusted to make the curve model highly consistent with the elastic part in the finite element analysis results, the knee part in the curve model and the finite element simulation results show a significant error.

$$M = M_u[1 - e^{\frac{-(K_i + c\theta)\theta}{M_u}}] \tag{56}$$

6.2. Proposed model

The analysis of the typical moment-rotation curve models shows that although the piecewise function model defines the elastic and ultimate parts appropriately, the knee part is not accurate enough and prone to mutation at the piecewise points, resulting in numerical problems such as non-convergence of calculation. On the other hand, the single nonlinear function model can obtain a continuous and smooth curve but lacks a clear definition of the elastic part and the ultimate part, which brings difficulties to analyzing the yield and ultimate load of joints. Considering the advantages and disadvantages of the existing typical moment-rotation curve representations, an improved moment-rotation curve representation is proposed in this paper, and its mathematical function is expressed in Eq. (57). The ratio of yield bending moment and ultimate bending moment α is introduced in this model so that $\theta_y = \alpha M_u / k_i$ is the yield rotation of joints. The definition of the elastic part refers to the trilinear model and the function model in Eurocode 3. The knee part is improved based on the three-parameter exponential function model so that the knee part is tangential to the elastic part at the piecewise point. Although the model does not clearly define the ultimate part of the joint, the curve model is obtained by the ultimate bending moment M_u, and $M = M_u$ is the asymptotic line. Therefore, it is feasible to

analyze the ultimate load of the joint even if the ultimate part is not clearly defined. In addition, the knee part of the curve model is determined by the exponential function with shape coefficient *c*, so the limit state of the joint can be considered by adjusting the shape coefficient to control the speed of the curve approaching the asymptotic line. To sum up, the suggested function model has high accuracy in the knee part while considering all force stages and avoiding numerical problems such as the non-convergence of calculation at the piecewise point. The moment-rotation curve model suggested in this paper is shown in Fig. 18.

$$M=\begin{cases} K_i\theta, & \theta \le \theta_y \\ \alpha M_u+(1-\alpha)M_u\left[1-e^{\frac{-[K_i+c(\theta-\theta_y)](\theta-\theta_y)}{(1-\alpha)M_u}}\right] & \theta > \theta_y \end{cases} \tag{57}$$

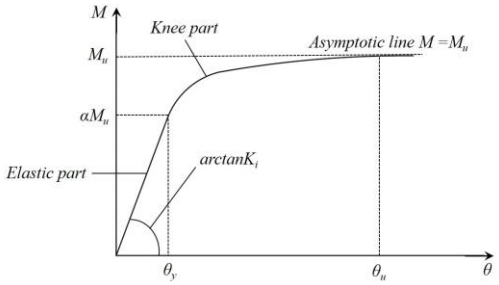

Fig. 18 The presented moment-rotation relationship model

The model recommended in this paper is utilized to calculate the moment-rotation curves of some beam-column joints with external cover plate in Table 2. In addition, the curves corresponding to the three typical models are presented in the same figure.The comparison of all curves is shown in Fig. 19. It is clear from this comparison that the curves calculated by the proposed model are well consistent with the finite element analysis results, which not only has the characteristics of high accuracy similar to a single nonlinear model in the knee part but also considers each force stage of the joint. In addition, the function model curve is continuous and smooth, which is convenient for subsequent structural analysis and calculation.

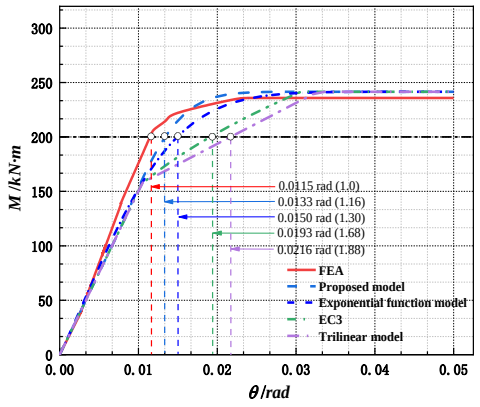

(a) BK260

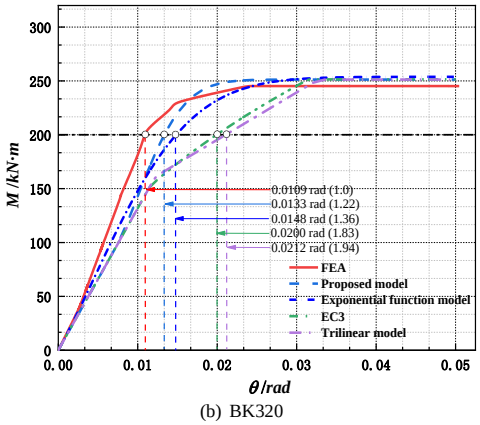

(b) BK320

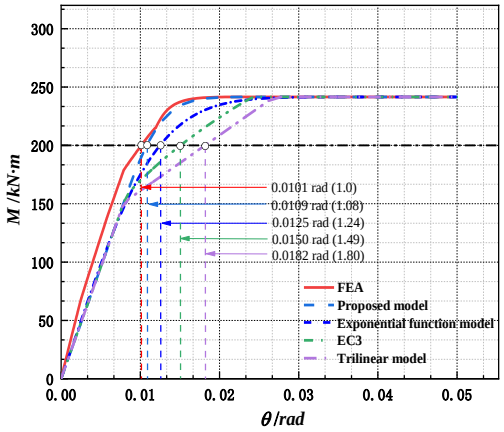

(c) BH15

Fig. 19 The moment-rotation curves determined by different models

7. Conclusions

In this paper, the force transmission mechanism of beam-column joints with the external cover plates was analyzed and the main force components of the joints were determined. The formulas for calculating the initial rotational stiffness and ultimate bending moment were supplied in accordance with the component analysis principle. On this basis, the moment-rotation curve model suitable for the external cover plate joint was proposed. From the study of this paper, The key findings may be summed up as follows:

(1) The equations for calculating the initial stiffness of this joint were established through the principle of the component method. The ratios between the predicted and actual findings from the numerical simulation had average and standard deviation values of 0.91 and 0.09, respectively, showing that the component analysis method can successfully predict the initial rotational stiffness of this joint.

(2) The various failure mechanisms of this joint were taken into consideration when developing the equations for the ultimate bending moment. The ratios between the predictions and the results of the numerical simulation had an average and standard deviation of 1.01 and 0.02, respectively, showing that the methods presented in this study can exactly determine the final moment resistance of this unique joint.

(3) The benefits of the previous piecewise and single nonlinear models are taken into consideration in the proposed model for the moment-roration relationship of beam-column joints. This model not only has a highly accurate knee part while considering each loading stage but also has smooth and continuous conditions at the piecewise points, which can avoid numerical problems such as non-convergence at the piecewise points in the subsequent analysis. Additionally, the moment-rotation curves derived by the suggested representation are in good agreement with the findings of the finite element analysis, showing that the suggested model is capable of properly projecting the mechanical behavior of the external cover plate joints.

Acknowledge

The authors sincerely acknowledge the financial support provided by the Key Project of the National Natural Science Foundation of China (No. 51938009) and the National Natural Science Foundation of China (No.51878419).

References

[1] Zhong S.T., The concrete-filled steel tubular structures, Beijing: Tsinghua University Press, 2003.
[2] Li G.C., Yu Y., Yang Z.J., Fang C., Ge H.B. and Liu Y.P., “Mechanical behavior of high-strength concrete filled high-strength steel tubular stub columns stiffened with encased I-shaped CFRP profile under axial compression”, Composite Structures, 275: 114504, 2021.
[3] Li G.C., Zhou B. and Pan J.H., “Finite element analysis on concrete-filled square steel tube short columns with inner CFRP profiles under axial compression”, Applied Mechanics and Materials, pp. 335-339, 2014.
[4] Feng X., Li G.C., Yang Z.J. and Cao W.Z., “Performance study on the mechanical behavior of a concrete-filled square steel tubular middle-long columns with inner I-shaped CFRP profiles under bi-axial eccentric loading”, Progress Steel Building Structures, 23(8):32-42+52, 2021. (in Chinese)
[5] Li W.Q., Chen Y.Y., Wang W., Xu Y.J. and Lv X.D., “Experimental study of external diaphragm joint connecting CHS column and H-shaped beam”, Advanced Steel Construction, 6(1): 578-588, 2010.
[6] Goswami R., Murty C.V.R., “Externally reinforced welded I-beam-to-box-column seismic connection”, Journal of Engineering Mechanics, 136(1), 23-30, 2010.
[7] Ye Q., Wang Y., Wang Z., Lin Y., Shu C. and Zhang F., “Experimental study of through diaphragm bolted joint between H-beam to CFST column”, Journal of Constructional Steel

Research, 182, 106647, 2021.
[8] Xu P.Z., Chen C., Yang L. and Zhu Y.G., “Finite element analysis on the seismic behavior of circular steel tubular column to H-shaped steel beam joint with cover-plate externally strengthened ring”, Progress in Steel Building Structures, 23(2): 14-21, 2021. (in Chinese)
[9] Cao S., Shu G., Lin K. and Qin Y., “Experimental seismic behaviour of bottom-through-diaphragm and top-ring connection to SST columns”, Journal of Constructional Steel Research, 150, 249-260, 2018.
[10] Wang W.D., Han L.H. and Uy B., “Experimental behaviour of steel reduced beam section to concrete-filled circular hollow section column connections”, Journal of Constructional Steel Research, 64(5), 493-504, 2008.
[11] Chen W.F., Torma S., Advanced Analysis in Steel Frames, Boca Raton: CRC Press, 1993.
[12] Masarira A., “The effect of joints on the stability behaviour of steel frame beams”, Journal of Constructional Steel Research, 58(10), 1375-1390, 2002.
[13] Faella C., Piluso V. and Rizzano G., Structural steel semirigid connections: Theory, Design and Software, Boca Raton, Florida: CRC Press LLC, 1999.
[14] Ding J.M., Shen Z.Y., “Influence of semi-rigid joint on internal force and displacement of steel frame structure”, Building Structure, 6, 8-12, 1991. (in Chinese)
[15] Wu F.H., Chen W.F., “A design model for semi-rigid connection”, Engineering Structures, 12(2), 88-97, 1990.
[16] Yee Y.L., Melchers R.E., “Moment-rotation curves for bolted connections”, Journal of Structural Engineering, 112(3), 615-635, 1986.
[17] Frye M., Morris G.A., “Analysis of flexibly connected steel frames”, Canadian Journal of Civi1 Engineering, 2(3), 280-291, 1975.
[18] Colson A., “Theoretical modeling of semirigid connections behavior”, Journal of Constructional Steel Research, 19(3), 213-224, 1991.
[19] Kishi N., Chen W.F., “Moment-rotation relation of semirigid connection with angles”, Journal of Structural Engineering, 116, 1813-1834, 1990.
[20] Ang K.M., Morris G.A., “Analysis of three-dimensional frames with flexible beam-column connections”, Canadian Journal of Civil Engineering, 11(2), 245-254, 1984.
[21] GB50017-2017, Steel Structure Design Standard. Beijing: China Construction Industry Press, 2017.
[22] GB50011-2010, Code for Seismic Design of Buildings. Beijing: China Construction Industry Press, 2016.
[23] JGJ99-2015, Technical Specification for High Rise Civil Steel Structures. Beijing: China Construction Industry Press, 2015.
[24] Han L.H., Concrete Filled Steel Tubular Structures: Theory and Practice. Beijing: Science Press, 2007.
[25] Li G.C., Zhan Z.C., Yang Z.J., Fang C. and Yang Y., “Behavior of concrete-filled square steel tubular stub columns stiffened with encased I-section CFRP profile under biaxial bending”, Journal of Constructional Steel Research, 169, 106065, 2020.
[26] Li G.C., Zhu Z.H., Sun X., Liu X.H. and Han Y.W., “Experimental research on concrete-filled square steel tubular slender columns with inner I-shaped CFRP under axial compression”, Journal of Building Structures, 38(S1), 226-232, 2017. (in Chinese)
[27] Zuo B., “Pseudo-static experimental study of H-shaped beams to cold-formed square steel tube columns connections with different outer diaphragm”, Qingdao Technological University, 2014. (in Chinese)
[28] Yuan Z.R., “The Research on the mechanical performance of the square concrete filled steel tube with T-stub connector”, Hunan University, 2013. (in Chinese)
[29] Liu H.C., Hao J.P., Xue Q. and Huang Y.Q., “Stress response and initial stiffness of side plate connections to WCFT columns”, Advanced Steel Construction, 17(3), 306-317, 2021.
[30] Zhao Q.W., Zhang S.M. and Jiang S.F., “Calculation model of initial rotational stiffness of steel beam-to-column bolted end-plate connections”, Engineering Mechanics, 26(6), 226-232, 2009. (in Chinese)
[31] Matsui C., “Strength and behavior of frames with concrete filled square steel tubular columns under earthquake loading”, Proceedings of the international specialty conference on concrete filled tubular structures, 104-111, 1985.
[32] EN1993-1-8, Eurocode 3: Design of Steel Structures - Part 1-8: Design of joints, 2010.
[33] Zhao J.H., Fan J.C. and Gao W.Q., “Moment-rotation analyses model of flush end-plate bolted connections between H-shape steel beams and rectangular CFST columns”, Engineering Mechanics, 38(6), 249-260, 2021. (in Chinese)